

# Data-Induced Interactions of Sparse Sensors

Andrei A. Klishin,<sup>1,2,\*</sup> J. Nathan Kutz,<sup>1,3</sup> and Krithika Manohar<sup>1,2</sup>

<sup>1</sup>*AI Institute in Dynamic Systems, University of Washington, Seattle, WA 98195, USA*

<sup>2</sup>*Department of Mechanical Engineering, University of Washington, Seattle, WA 98195, USA*

<sup>3</sup>*Departments of Applied Mathematics and Electrical and Computer Engineering,  
University of Washington, Seattle, WA 98195, USA*

(Dated: July 25, 2023)

Large-dimensional empirical data in science and engineering frequently has low-rank structure and can be represented as a combination of just a few eigenmodes. Because of this structure, we can use just a few spatially localized sensor measurements to reconstruct the full state of a complex system. The quality of this reconstruction, especially in the presence of sensor noise, depends significantly on the spatial configuration of the sensors. Multiple algorithms based on gappy interpolation and QR factorization have been proposed to optimize sensor placement. Here, instead of an algorithm that outputs a singular “optimal” sensor configuration, we take a thermodynamic view to compute the full landscape of sensor interactions induced by the training data. The landscape takes the form of the Ising model in statistical physics, and accounts for both the data variance captured at each sensor location and the crosstalk between sensors. Mapping out these data-induced sensor interactions allows combining them with external selection criteria and anticipating sensor replacement impacts.

Many natural and engineered systems can take a variety of high-dimensional states, with the amount of data growing rapidly with the number of observed snapshots and increasing snapshot resolution. At the same time, the amount of information in this data usually grows much slower, often logarithmically [1–3]. In this situation, any system state can be closely approximated by a combination of just a few basis vectors, enabling algorithms from lossy image compression to Dynamic Mode Decomposition [4, 5]. While the optimal basis can be learned from historical data or high-fidelity simulations, states cannot be measured in that basis directly and often can only be accessed by spatially-localized sensors.

Reconstruction of full states from localized sensor measurements has a long history under the umbrella term of *compressed sensing*, where the sampling points (sensor locations) are chosen randomly and the state is reconstructed as a sparse combination of universal basis vectors [6–8]. More recently, driven by advances in gappy and reduced-order PDE methods [9–11], *sparse sensing* algorithms have been developed to take advantage of the available training data to reduce the number of sensors required for given reconstruction quality [12]. The general sparse sensing problem is usually set up as follows: given the training data matrix  $X$  consisting of  $N$  snapshots of an  $n$ -dimensional state, one needs to reconstruct an unknown state  $\vec{x} \in \mathbb{R}^n$  sampled from the same distribution as the data by using only the noisy measurements of a few components of the state  $\vec{y} \in \mathbb{R}^p$ ,  $p \ll n$ .

While any combination of sensors of appropriate rank can be used to compute the maximal likelihood state reconstruction, the reconstruction robustness to sensor noise may vary by orders of magnitude, leading to the problem of *sensor placement*. Each sensor configuration can be assigned a cost function value that can be approximately maximized with efficient greedy heuristics

based on optimal experiment design, information theory metrics, Gibbs sampling, or matrix QR pivoting [12–16]. While these methods return a sensor configuration provably close to the true optimum due to the submodularity property [17–19], they do not inform why a particular configuration should be chosen, how to best modify it if sensor budget changes, and what would be the impact of a sensor malfunction on the reconstruction quality.

In this paper, instead of searching for a singular “optimal” configuration of sensors, we take a thermodynamic perspective to study the entire landscape of sensor interactions, akin to saliency maps in machine vision [20]. We show that the sensor interactions can be interpreted in terms of 1-body, 2-body, and higher order Hamiltonian terms computed directly from the training data. Understanding the part of the landscape induced by data directly inspires a greedy sensor placement algorithm, allows incorporating landscapes driven by external cost factors, and anticipates the impacts of sensor replacement needs. The energy landscape analysis can be combined with other recent advances in sensor placement studies.

*State reconstruction algorithm.* The training library can be represented via Proper Orthogonal Decomposition (POD) and closely approximated via POD truncation:

$$X = \Psi \Sigma V^T \approx \Psi_r \Sigma_r V_r^T, \quad (1)$$

where we dropped all singular values beyond the first  $r$  per the optimal truncation prescription [3]. In the reduced basis any state can be approximated as a linear combination of data-driven basis vectors  $\vec{x} \approx \Psi_r \vec{a}$ .

Our goal is to estimate the coefficients  $\hat{\vec{a}}$  from the spatially-localized measurements  $\vec{y} = C\vec{x} + \xi$ , where  $C$  is a  $p \times n$  *selection matrix* consisting of  $p$  rows of the identity matrix and  $\xi$  is Gaussian uncorrelated sensor measurement noise with magnitude  $\eta$ . Given this measurement model and a Gaussian prior distribution of the

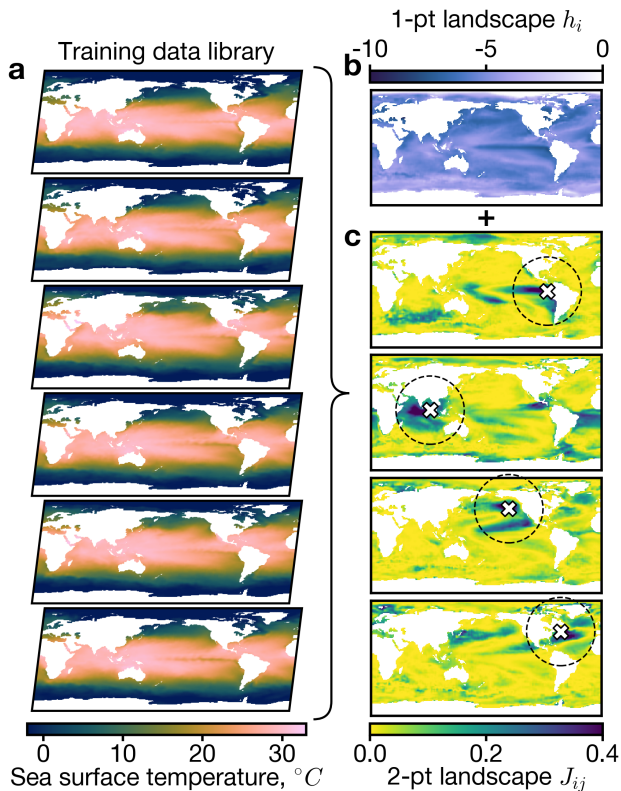


FIG. 1. Computation of the sensor placement landscape from the training data library. (a) A collection of data snapshots of identical dimensions, here the Sea Surface Temperature data set. (b) The library is used to compute the sensor placement landscape to multiple orders, here showing the 1-point landscape at each location  $h_i$  and the 2-point landscape  $J_{ij}$  conditioned on the sensor locations marked with white crosses and highlighted with dashed circles.

coefficients  $\vec{a}$  parameterized by the variances  $S$ , we derive the following maximal likelihood reconstruction:

$$\hat{\vec{a}} = \left( S^{-2} + \frac{\Theta^T \Theta}{\eta^2} \right)^{-1} \frac{\Theta^T \vec{y}}{\eta^2} = A^{-1} \frac{\Theta^T \vec{y}}{\eta^2}; \hat{\vec{x}} = \Psi_r \hat{\vec{a}} \quad (2)$$

valid for any choice of sensors  $C$  and sensor readings  $\vec{y}$ , with  $\Theta = C\Psi_r$ . However, the accuracy and noise sensitivity of this reconstruction depend dramatically on the properties of the sensor-dependent matrix  $A$ , and thus requires a strategy to place sensors systematically.

*Sensor placement landscapes.* The reconstruction error of Eqn. 2 can be measured by various scalar functions of the matrix  $A$ , most commonly its determinant, in an approach known as D-optimal design [13]. The determinant is an attractive optimization target because it characterizes the uncertainty hypervolume of the reconstruction, its maximum can be approximated with the QR decomposition [12], and the submodularity property guarantees the near-optimality of greedy optimiza-

tion [17–19].

In this paper we identify the (negative) determinant of the inversion matrix with the energy or Hamiltonian of a particular set of sensors  $\gamma$ . The resulting Hamiltonian is remarkably similar to the Ising model found across statistical physics:

$$\mathcal{H}(\gamma) \equiv -\ln(\det A) \approx E_b + \sum_{i \in \gamma} h_i + \sum_{i \neq j \in \gamma} J_{ij} \quad (3)$$

$$h_i \equiv -\ln(1 + \vec{g}_i \cdot \vec{g}_i / \eta^2) \leq 0 \quad (4)$$

$$J_{ij} \equiv \frac{1}{2} \frac{(\vec{g}_i \cdot \vec{g}_j / \eta^2)^2}{(1 + \vec{g}_i \cdot \vec{g}_i / \eta^2)(1 + \vec{g}_j \cdot \vec{g}_j / \eta^2)} \geq 0, \quad (5)$$

where  $\vec{g}_i$  are the *sensing vectors* describing the sensitivity of each possible sensor location to each of the POD modes, computed as rows of the data-driven matrix  $G = \Psi_r S$ . The functional form of  $h_i$  and  $J_{ij}$  is computed via series expansion of the matrix  $A$  in powers of  $\eta$  (Eqn. 2) and resummation, similar to enumeration arguments in self-assembly studies [21, 22] (see Supplementary Materials for derivation).

In the Hamiltonian formulation of sensor placement 3, the objective depends on the locations of individual sensors and sensor pairs from the chosen set  $\gamma$  (Fig. 1). Qualitatively, minimizing the Hamiltonian requires picking sensors  $i \in \gamma$  that capture a lot of signal variance (large  $\vec{g}_i \cdot \vec{g}_i$ ), but are not very correlated with each other (small  $\vec{g}_i \cdot \vec{g}_j$ ). While a combinatorial search for the lowest energy configuration would require evaluating the  $\mathcal{O}(n^2)$  elements of the full crosstalk  $\mathbf{J}$  matrix, we propose a simple greedy “2-point” algorithm that minimizes the marginal energy of each next placed sensor:

$$q = \arg \min_q \left( h_q + 2 \sum_{i \in \gamma} J_{iq} \right); \gamma \leftarrow q, \quad (6)$$

requiring just  $\mathcal{O}(p \cdot n)$  evaluations to place  $p \ll n$  sensors.

*Reconstruction progress.* We demonstrate the sensor placement algorithm on an example dataset of weekly average sea surface temperature (SST) between 1990 and 2023 [23], truncated to POD rank  $r = 100$ . Each frame covers the entirety of Earth surface in equirectangular projection at  $1^\circ$  resolution, resulting in  $360 \times 180$  pixel images with  $n = 44219$  pixels corresponding to sea surface. We show that by employing as few as 25 sensors selected by the 2-point algorithm with noise level of  $\eta = 1^\circ\text{C}$ , the entire temperature field can be reconstructed to within  $1^\circ\text{C}$  (Fig. 2a). The reconstruction method also provides an Uncertainty Quantification (UQ) method in form of the uncertainty heat map at every pixel (Fig. 2b). Uncertainty is lowest close to the selected sensors, primarily around continents and within inland bodies of water, and highest in southern parts of the Indian, Pacific, and Atlantic Oceans. We emphasize that the sensor placement algorithm was trained exclusively on the snapshot

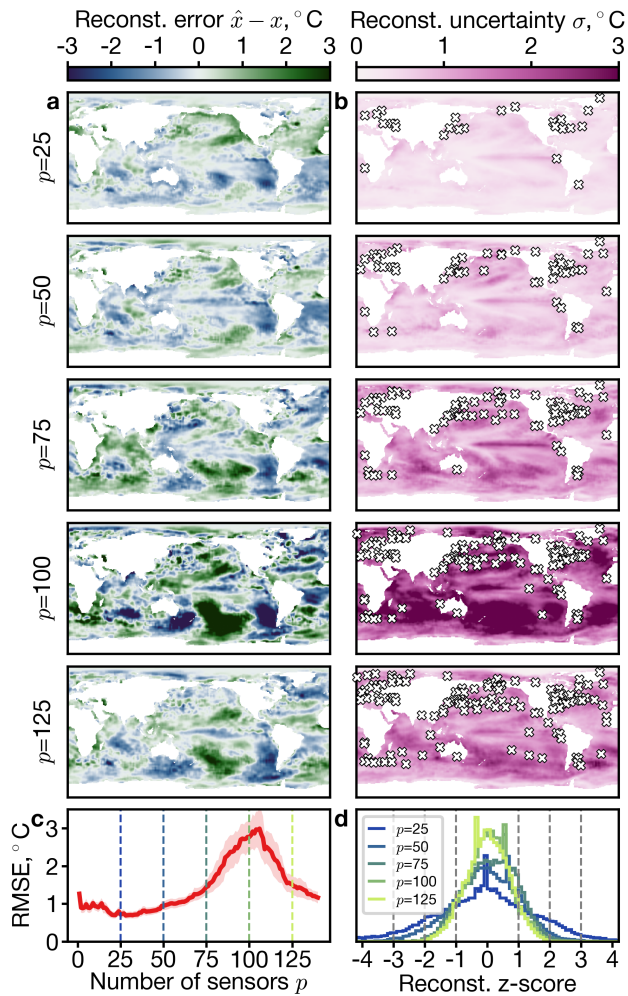


FIG. 2. State reconstruction with progressively more sensors  $p$  at noise level  $\eta = 1.0^{\circ}\text{C}$ . (a) Reconstruction error between the maximal likelihood reconstructed state and the true state. (b) Uncertainty heatmaps of the reconstruction and the sensor locations chosen by the 2-point algorithm (white crosses). (c) RMSE of the reconstruction with the solid curve and the shaded region showing mean  $\pm$  one standard deviation across 20 realizations of sensor noise. The RMSE peak corresponds to the model dimension, here  $r = 100$ . (d) Distribution of reconstruction z-scores at every pixel  $z_i = (\hat{x}_i - x_i)/\sigma_i$

library, with no additional information about the structure of Earth’s oceans or their physical processes.

The reconstruction Root Mean Square Error (RMSE) shows non-monotonic dependence on the number of sensors (Fig. 2c). While adding more sensors contributes more information to the reconstruction algorithm, it also trades off with the number of independent sources of noise, resulting in best performance at  $p \sim 25$  for sensor noise of  $\eta = 1.0^{\circ}\text{C}$ . Importantly, the RMSE peaks at  $p \sim r = 100$  since the model cannot reconstruct the features in the truncated POD modes. Since both the

reconstruction error and reconstruction uncertainty increase with sensor number, we assess the model confidence by computing the z-score of each individual pixel  $z_i = (\hat{x}_i - x_i)/\sigma_i$  and plotting its distribution (Fig. 2d). Across all sensor numbers, the z-score distribution is symmetric and concentrated within  $z \in [-3, 3]$ , indicating that the reconstruction does not systematically over- or under-estimate the temperature, and provides an accurate estimation of the uncertainty.

*Reconstruction diagnostics* We compute sensor placement and reconstruction error across five datasets and four sensor placement methods. Apart from the SST dataset, we use the Olivetti faces dataset [24], snapshots of a numerical simulation of flow past a cylinder [25, 26], as well as synthetic Gaussian Free Field [27] and Random State System [28] datasets (Fig. 3a, see SM for dataset details). The four sensor placement algorithms are: random, 1-point (minimizing  $h_q$  only), 2-point (Eqn. 6), and QR-based [29]. For the QR sensors, we compute reconstruction with and without the prior regularization. For each dataset, the sensor placement landscape is derived from the training set with 80% of the data, and the reconstruction error is computed across the test set with the remaining 20% of the data.

For the three empirical datasets (SST, Olivetti, and cylinder) the random and 1-point algorithms have higher energies than the other two (Fig. 3b). The 1-point algorithm has higher RMSE than other reconstructions with prior, highlighting the importance of crosstalk for sensor placement (Fig. 3c). The QR sensors without prior regularization also show consistently higher RMSE, justifying the need for a prior. The regularized random, 2-point, and QR algorithms show nearly equivalent RMSE error curves, all showing the peak at  $p \sim r$  due to the POD mode truncation. For the two synthetic datasets all sensor placement methods have nearly equivalent performance, but can also be compared to brute force search (see SM). We conclude that while the 2-point and the QR algorithms are based on the same underlying POD modes and have nearly equivalent numerical performance, the 2-point algorithm provides much richer interpretation in terms of sensor landscapes and interactions.

*Conclusions and outlook.* The key advance of this paper is casting the sensor selection problem in thermodynamic terms of interaction energies of progressively larger numbers of sensors. While we focus the discussion on the 1-body and 2-body interactions, the mathematical formalism extends to any higher number (see SM). The shape of the 2-body interactions can be further connected to the properties of the physical, mathematical, or even artistic processes that generate data [30–32]. We used a greedy 2-point method of sensor placement in order to limit the required memory and computing time, but if the whole landscape could fit in memory, better energy minima can be obtained through methods such as gradient descent or simulated annealing [33]. Due to the usage

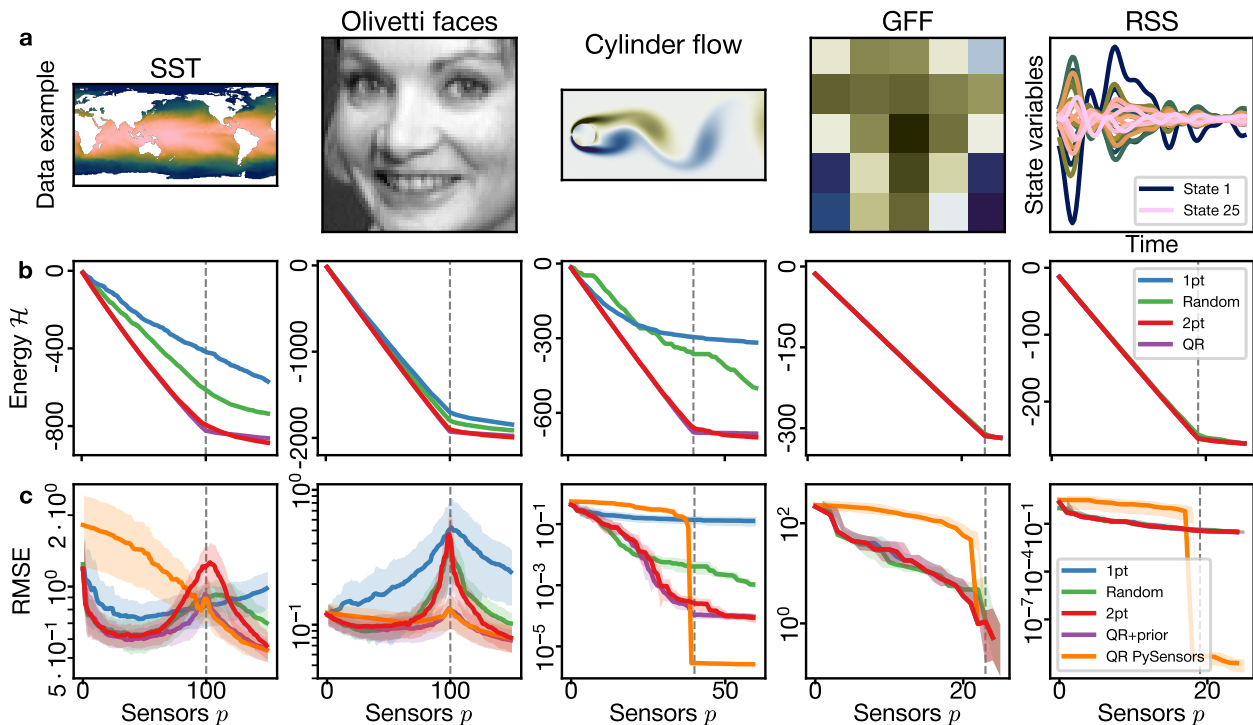


FIG. 3. Comparison of reconstruction metrics for different datasets, with 4:1 train/test split. (a) Examples of dataset snapshots for different systems. The RSS dataset is non-spatial, so temporal trajectories are shown instead. (b) Exact energies of sensor configurations selected with different methods: random placement, 1-point algorithms, 2-point algorithm, and QR pivoting. (c) Root mean square error (RMSE) of state reconstruction, with solid line and shaded region indicating average  $\pm 1$  standard deviation across the test set. The vertical dashed line indicates the number of modes  $r$  used in the reconstruction.

of a regularizing prior, state reconstruction can be consistently performed for any number of sensors without the requirement that  $p \geq r$  [12].

While the sensor landscape approach provides interpretability and in some regimes selects better sensor sets than state-of-the-art approaches, it is ultimately followed by a *linear* algorithm for reconstructing the state from sensor readings, limiting the reconstruction accuracy. Recent work has shown that a linear algorithm of sensor selection based on QR factorization can be combined with a nonlinear shallow decoder network state estimation, which nevertheless requires neural network retraining for any new sensor set [34]. An alternative approach instead focuses on learning the data manifold geometry and identifying nonlinear coordinates [19], which would be equivalent to replacing the Gaussian prior in our approach with a more complex one. Other sensor placement extensions can involve estimation of time-dependent dynamics through Kalman filtering [35], or sensors advected by the flows they are trying to measure [36]. Finally, the approach here identifies only the part of sensor placement landscape induced by the training data, which can be combined with other design objectives such as placement cost or restrictions [37–40].

The authors would like to thank S.E. Otto and J. Williams for helpful discussions and L.D. Lederer for administrative support. This work uses Scientific Color Maps for visualization [41]. The authors acknowledge support from the National Science Foundation AI Institute in Dynamic Systems (grant number 2112085).

\* aklishin@uw.edu

- [1] K. N. Quinn, M. C. Abbott, M. K. Transtrum, B. B. Machta, and J. P. Sethna, Information geometry for multiparameter models: New perspectives on the origin of simplicity, *Reports on Progress in Physics* (2022).
- [2] M. Udell and A. Townsend, Why are big data matrices approximately low rank?, *SIAM Journal on Mathematics of Data Science* **1**, 144 (2019).
- [3] M. Gavish and D. L. Donoho, The optimal hard threshold for singular values is  $4/\sqrt{3}$ , *IEEE Transactions on Information Theory* **60**, 5040 (2014).
- [4] J. N. Kutz, S. L. Brunton, B. W. Brunton, and J. L. Proctor, *Dynamic mode decomposition: data-driven modeling of complex systems* (SIAM, 2016).
- [5] A. S. Lewis and G. Knowles, Image compression using the 2-d wavelet transform, *IEEE Transactions on image*

- Processing **1**, 244 (1992).
- [6] D. L. Donoho, Compressed sensing, *IEEE Transactions on information theory* **52**, 1289 (2006).
- [7] S. Ganguli and H. Sompolinsky, Statistical mechanics of compressed sensing, *Physical review letters* **104**, 188701 (2010).
- [8] F. Krzakala, M. Mézard, F. Sausset, Y. Sun, and L. Zdeborová, Statistical-physics-based reconstruction in compressed sensing, *Physical Review X* **2**, 021005 (2012).
- [9] R. Everson and L. Sirovich, Karhunen–loève procedure for gappy data, *JOSA A* **12**, 1657 (1995).
- [10] M. Barrault, Y. Maday, N. C. Nguyen, and A. T. Patera, An ‘empirical interpolation’ method: application to efficient reduced-basis discretization of partial differential equations, *Comptes Rendus Mathématique* **339**, 667 (2004).
- [11] S. Chaturantabut and D. C. Sorensen, Discrete empirical interpolation for nonlinear model reduction, in *Proceedings of the 48th IEEE Conference on Decision and Control (CDC) held jointly with 2009 28th Chinese Control Conference* (IEEE, 2009) pp. 4316–4321.
- [12] K. Manohar, B. W. Brunton, J. N. Kutz, and S. L. Brunton, Data-driven sparse sensor placement for reconstruction: Demonstrating the benefits of exploiting known patterns, *IEEE Control Systems Magazine* **38**, 63 (2018).
- [13] P. F. de Aguiar, B. Bourguignon, M. Khots, D. Massart, and R. Phan-Thau-Luu, D-optimal designs, *Chemometrics and intelligent laboratory systems* **30**, 199 (1995).
- [14] A. Krause, A. Singh, and C. Guestrin, Near-optimal sensor placements in gaussian processes: Theory, efficient algorithms and empirical studies., *Journal of Machine Learning Research* **9** (2008).
- [15] H. Sun, A. V. Dalca, and K. L. Bouman, Learning a probabilistic strategy for computational imaging sensor selection, in *2020 IEEE International Conference on Computational Photography (ICCP)* (IEEE, 2020) pp. 1–12.
- [16] B. Peherstorfer, Z. Drmac, and S. Gugercin, Stability of discrete empirical interpolation and gappy proper orthogonal decomposition with randomized and deterministic sampling points, *SIAM Journal on Scientific Computing* **42**, A2837 (2020).
- [17] G. L. Nemhauser, L. A. Wolsey, and M. L. Fisher, An analysis of approximations for maximizing submodular set functions—i, *Mathematical programming* **14**, 265 (1978).
- [18] A. Krause and C. Guestrin, Submodularity and its applications in optimized information gathering, *ACM Transactions on Intelligent Systems and Technology (TIST)* **2**, 1 (2011).
- [19] S. E. Otto and C. W. Rowley, Inadequacy of linear methods for minimal sensor placement and feature selection in nonlinear systems: a new approach using secants, *Journal of Nonlinear Science* **32**, 69 (2022).
- [20] K. Simonyan, A. Vedaldi, and A. Zisserman, Deep inside convolutional networks: Visualising image classification models and saliency maps, arXiv preprint arXiv:1312.6034 (2013).
- [21] A. Murugan, J. Zou, and M. P. Brenner, Undesired usage and the robust self-assembly of heterogeneous structures, *Nature communications* **6**, 6203 (2015).
- [22] A. A. Klishin and M. P. Brenner, Topological design of heterogeneous self-assembly, arXiv preprint arXiv:2103.02010 (2021).
- [23] B. Huang, C. Liu, V. Banzon, E. Freeman, G. Graham, B. Hankins, T. Smith, and H.-M. Zhang, Improvements of the daily optimum interpolation sea surface temperature (doisst) version 2.1, *Journal of Climate* **34**, 2923 (2021).
- [24] F. S. Samaria and A. C. Harter, Parameterisation of a stochastic model for human face identification, in *Proceedings of 1994 IEEE workshop on applications of computer vision* (IEEE, 1994) pp. 138–142.
- [25] K. Taira and T. Colonius, The immersed boundary method: a projection approach, *Journal of Computational Physics* **225**, 2118 (2007).
- [26] T. Colonius and K. Taira, A fast immersed boundary method using a nullspace approach and multi-domain far-field boundary conditions, *Computer Methods in Applied Mechanics and Engineering* **197**, 2131 (2008).
- [27] C. Cadiou, Fyeldgenerator (2022).
- [28] S. Fuller, B. Greiner, J. Moore, R. Murray, R. van Paassen, and R. Yorke, The python control systems library (python-control), in *2021 60th IEEE Conference on Decision and Control (CDC)* (IEEE, 2021) pp. 4875–4881.
- [29] B. M. de Silva, K. Manohar, E. Clark, B. W. Brunton, S. L. Brunton, and J. N. Kutz, Pysensors: A python package for sparse sensor placement, arXiv preprint arXiv:2102.13476 (2021).
- [30] G. J. Stephens, T. Mora, G. Tkačik, and W. Bialek, Statistical thermodynamics of natural images, *Physical review letters* **110**, 018701 (2013).
- [31] B. Duplantier, R. Rhodes, S. Sheffield, and V. Vargas, Log-correlated gaussian fields: an overview, *Geometry, Analysis and Probability: In Honor of Jean-Michel Bismut*, 191 (2017).
- [32] J. Kent-Dobias, Log-correlated color in monet’s paintings, arXiv preprint arXiv:2209.01989 (2022).
- [33] S. Kirkpatrick, C. D. Gelatt Jr, and M. P. Vecchi, Optimization by simulated annealing, *science* **220**, 671 (1983).
- [34] J. Williams, O. Zahn, and J. N. Kutz, Data-driven sensor placement with shallow decoder networks, arXiv preprint arXiv:2202.05330 (2022).
- [35] V. Tzoumas, A. Jadbabaie, and G. J. Pappas, Sensor placement for optimal kalman filtering: Fundamental limits, submodularity, and algorithms, in *2016 American Control Conference (ACC)* (IEEE, 2016) pp. 191–196.
- [36] S. Shrivastava, G. Snyder, and Z. Song, Dynamic compressed sensing of unsteady flows with a mobile robot, in *2022 IEEE/RSJ International Conference on Intelligent Robots and Systems (IROS)* (IEEE, 2022) pp. 11910–11915.
- [37] A. A. Klishin, C. P. Shields, D. J. Singer, and G. van Anders, Statistical physics of design, *New Journal of Physics* **20**, 103038 (2018).
- [38] E. Clark, T. Askham, S. L. Brunton, and J. N. Kutz, Greedy sensor placement with cost constraints, *IEEE Sensors Journal* **19**, 2642 (2018).
- [39] T. Nishida, N. Ueno, S. Koyama, and H. Saruwatari, Region-restricted sensor placement based on gaussian process for sound field estimation, *IEEE Transactions on Signal Processing* **70**, 1718 (2022).
- [40] N. Karnik, M. G. Abdo, C. E. E. Perez, J. S. Yoo, J. J. Cogliati, R. S. Skifton, P. Calderoni, S. L. Brunton, and K. Manohar, Optimal sensor placement with adaptive constraints for nuclear digital twins (2023), arXiv:2306.13637 [math.OC].
- [41] F. Cramer, Scientific colour maps (2023).

# Data-Induced Interactions of Sparse Sensors: Supplementary Materials

Andrei A. Klishin,<sup>\*</sup> J. Nathan Kutz, and Krithika Manohar  
(Dated: July 25, 2023)

## S1. DATA PREPROCESSING

### A. Sea Surface Temperature

The Sea Surface Temperature (SST) dataset is curated by the National Oceanic and Atmospheric Administration (NOAA) and employs the Optimal Interpolation (OI) method to collect observations from different platforms and places them on a single regular grid for long periods of observations [1]. In this work we use OISST 2.0 dataset [2] that has the spatial resolution of 1 degree in both latitude and longitude, and is temporally averaged for each week between Dec 31, 1989 and Jan 1, 2023 for a total of  $N = 1727$  snapshots. Each temperature snapshot is given in equirectangular projection of size  $360 \times 180$  pixels. All of land surface of Earth is excluded from observations via a time-independent binary mask, leaving  $n = 44219$  pixels that vary between the states. We center the dataset by subtracting the temporal mean temperature profile from each snapshot. The POD is truncated to rank  $r = 100$ ,

### B. Olivetti faces

The Olivetti faces dataset consists of photos of individuals taken between April 1992 and April 1994 at AT&T Laboratories Cambridge [3]. Each of 40 individuals has 10 images, for a total of  $N = 400$  presented in random order. Each photo has the size  $64 \times 64$  grayscale pixels, resulting in  $n = 4096$ . We center each image both locally and globally by subtracting the mean brightness value of each image and the mean value across the dataset. The POD is truncated to rank  $r = 100$ .

### C. Cylinder flow

The cylinder flow dataset consists of scalar vorticity fields in 2D flow of a liquid around a cylinder, numerically simulated with immersed boundary method in Refs. [4, 5]. In the simulation regime at Reynolds number  $Re = 100$ , the flow consists of periodic shedding of vortices from the two sides of the cylinder in alternating order. The data consists of  $N = 151$  snapshots of resolution  $449 \times 199$  pixels, resulting in data dimension

$n = 89351$ . We center the data by subtracting the temporal average vorticity profile from each snapshot. The POD is truncated to rank  $r = 40$ .

### D. Gaussian Free Field

The Gaussian Free Field (GFF) dataset is generated synthetically with the FyeldGenerator package [6]. The field is generated by drawing pseudorandom values of Fourier modes according to a user-specified power spectrum. In order to ensure that the field has coarse features on small spatial scale, we chose power spectrum  $P(k) \propto k^{-10}$  as opposed to the usual  $P(k) \propto k^{-2}$  for standard GFF. We generated  $N = 50$  pseudorandom snapshots of a field in the spatial domain  $5 \times 5$  pixels, resulting in  $n = 25$ . The small size of the synthetic dataset was required to enable the exhaustive enumeration of sensors, see Sec. S10. We center each image both locally and globally by subtracting the mean brightness value of each image and the mean value across the dataset. The POD is truncated to rank  $r = 23$ , equal to the number of singular values above machine precision  $\sigma > 10^{-15}$ .

### E. Random State System

The Random State System (RSS) dataset is generated synthetically with the Python Control Package [7] that replicates the functionality of Matlab Control Toolbox. RSS is a linear dynamical system with equation  $\dot{\vec{x}} = M\vec{x}$  for a random square matrix  $M$  of specified dimension, which we choose to be  $n = 25$ . The generating package does not request any other free parameters such as the distribution of the random matrix, other than ensuring the dynamical system stability, i.e.  $\forall \lambda : Re(\lambda) \leq 0$ . We obtain the trajectory data by initializing random iid initial condition  $x_i(t = 0) \sim \mathcal{N}(0, 1)$  and integrating the dynamical equation numerically in the range  $t \in [0, 5]$ , sampling  $N = 101$  snapshots. The small size of the synthetic dataset was required to enable the exhaustive enumeration of sensors, see Sec. S10. We center each state both locally and globally by subtracting the mean brightness value of each image and the mean value across the dataset. The POD is truncated to rank  $r = 19$ , equal to the number of singular values above machine precision  $\sigma > 10^{-15}$ .

<sup>\*</sup> aklishin@uw.edu

## F. Dataset singular values

Fig. S1 shows the spectra of singular values for each of the five datasets, along with the truncation threshold. As expected, singular values span many orders of magnitude for both empirical and synthetic datasets.

## S2. PRIOR AND STATE RECONSTRUCTION

### A. Bayesian inference

Here we situate state reconstruction as a problem of Bayesian inference from noisy sensor data. We place  $p \ll n$  sensors each measuring the scalar field in one location. We denote the set of sensors as  $\gamma$ , the set of sensor location indices. Given a full  $n$ -dimensional state vector  $\vec{x}$ , the sensor output is a much shorter state vector, sometimes called gapped [8]:

$$\vec{y} = C\vec{x} = C\Psi_r\vec{a} = \Theta\vec{a}, \quad (\text{S1})$$

where  $C$  is a  $p \times n$  sensor selector matrix with the entry 1 for the location that each sensor measures, and 0 otherwise. The matrix  $\Theta : p \times r$  combines the sensor selection with the low-rank representation of the scalar field.

We further assume that each sensor measures the scalar field with a Gaussian noise of magnitude  $\eta$ . Thus, given a true state  $\vec{a}$ , the probability distribution of sensor readings is given by:

$$p(\vec{y}|\vec{a}) \propto \exp\left(-\frac{(\vec{y} - \Theta\vec{a})^2}{2\eta^2}\right), \quad (\text{S2})$$

where we omit the distribution normalization.

For Bayesian inference, we invert the distribution using the Bayes rule:

$$p(\vec{a}|\vec{y}) = \frac{p(\vec{y}|\vec{a})p(\vec{a})}{p(\vec{y})}, \quad (\text{S3})$$

where  $p(\vec{a})$  is a *prior* distribution and  $p(\vec{y})$  is a normalization. The procedure of state estimation consists of computing the Maximum A Posteriori (MAP) estimate, which is typically done on log-likelihood:

$$\hat{\vec{a}} = \arg \max_{\vec{a}} (\ln p(\vec{y}|\vec{a}) + \ln p(\vec{a})), \quad (\text{S4})$$

where the normalization  $p(\vec{y})$  was omitted as it doesn't depend on the inferred state  $\vec{a}$ . The solution of this argmax problem requires knowing the functional form of the prior that we discuss below.

### B. Constructing the prior

In order to exploit the prior information of the data, we need to assume a functional form of the prior distribution

over the coefficients  $\vec{a}$ . A simple form of this assumption is to select a Gaussian prior of form:

$$p_{\text{Gauss}}(\vec{a}) \propto \exp\left(-\frac{\vec{a}^T S^{-2} \vec{a}}{2}\right), \quad (\text{S5})$$

which poses that the system states are drawn from an anisotropic Gaussian cloud where the variances along each orthogonal direction are given by the elements of a diagonal matrix  $S$ . We consider two choices for the prior: a scaled identity matrix  $S = \sigma I_r$  for uniform variance along all dimensions, and the matrix of singular values of the training data  $S = \Sigma_r$  for hierarchically decreasing variance of higher modes. Since in both cases all  $r$  elements are positive, the  $S$  matrix is invertible and thus the prior is normalizable. In this case the prior functions as a regularizer of state reconstruction. More complex prior distributions can be constructed for training data situated on curved manifolds [9].

### C. Gaussian prior inference

For the Gaussian functional form of the prior (Eqn. S5), we explicitly write out the log-likelihood as follows:

$$\ln p(\vec{a}|\vec{y}) = -\frac{1}{2\eta^2} (\vec{y} - \Theta\vec{a})^T (\vec{y} - \Theta\vec{a}) - \frac{\vec{a}^T S^{-2} \vec{a}}{2}, \quad (\text{S6})$$

which is a quadratic function of the unknown state  $\vec{a}$ .

The reconstruction is obtained by setting the  $\vec{a}$ -derivative to zero:

$$\frac{\partial \ln p(\vec{a}|\vec{y})}{\partial \vec{a}} = \frac{\Theta^T \vec{y}}{\eta^2} - \frac{\Theta^T \Theta \vec{a}}{\eta^2} - S^{-2} \vec{a} = 0, \quad (\text{S7})$$

which results in a simple linear equation for state reconstruction. Solving the equation, we get the following prescription for reconstruction:

$$\hat{\vec{a}} = \left(S^{-2} + \frac{\Theta^T \Theta}{\eta^2}\right)^{-1} \frac{\Theta^T \vec{y}}{\eta^2} = A^{-1} \frac{\Theta^T \vec{y}}{\eta^2}, \quad (\text{S8})$$

which combines the information from the prior and the sensors. This reconstruction is linear and works for any values of sensor measurements  $\vec{y}$ , and thus does not say which set of sensors is better or worse and thus does not guide our sensor selection.

The reconstruction depends on inverting the composite matrix  $A$ , which might be ill-conditioned, meaning that small errors or noise in sensor measurements  $\vec{y}$  can result in large error in the reconstructed state. We thus need to connect the reconstruction uncertainty to the metrics of matrix condition. Once such a metric is formulated, sensor placement can be designed to optimize it.

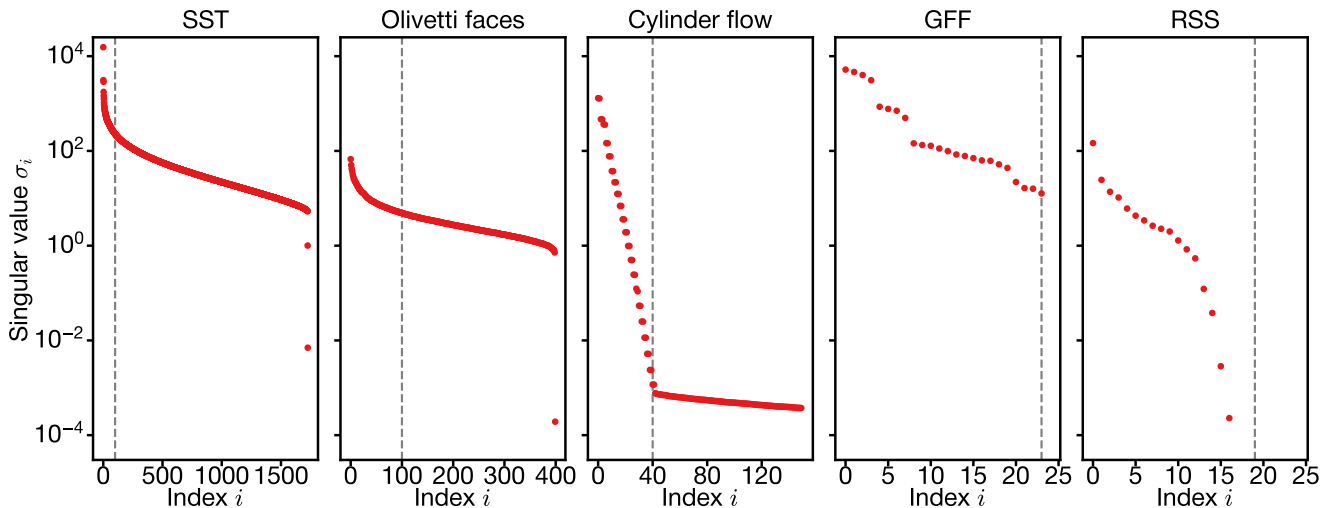


FIG. S1. Singular values of the five datasets used. Gray dashed line indicates the POD truncation threshold chosen for each of the datasets.

### S3. RECONSTRUCTION UNCERTAINTY HEATMAP

The reconstruction formula (S8) gives the maximal likelihood state, but the uncertainty around that state is non-uniformly distributed. In order to quantify the uncertainty, here we compute the uncertainty heatmap across the whole domain of  $\vec{x}$ , given the sensor placement  $C$ . We denote the sensor reading fluctuation as  $\vec{\Delta y}$ , and propagate that fluctuation to the state reconstruction:

$$\vec{\Delta x} = \Psi_r A^{-1} \frac{\Theta^T}{\eta^2} \vec{\Delta y}. \quad (\text{S9})$$

The state fluctuation depends on the realization of sensor noise, which needs to be averaged out. We can compute the average covariance matrix between all the entries of  $\vec{\Delta x}$  by taking the outer product of the state fluctuation with itself:

$$\langle \vec{\Delta x} \vec{\Delta x}^T \rangle = \Psi_r A^{-1} \frac{\Theta^T}{\eta^2} \langle \vec{\Delta y} \vec{\Delta y}^T \rangle \frac{\Theta}{\eta^2} A^{-1} \Psi_r^T, \quad (\text{S10})$$

where the sensor reading covariance is  $\langle \vec{\Delta y} \vec{\Delta y}^T \rangle = I_p \eta^2$  by the assumption of uncorrelated noise. The whole state covariance matrix is  $n \times n$ , which characterizes uncertainty correlations between different locations but does not easily fit in computer memory for large state spaces.

We instead compute only the diagonal part of the covariance matrix, characterizing the level of uncertainty in each pixel of the reconstructed state:

$$B \equiv \Psi_r A^{-1} \frac{\Theta^T}{\eta^2} \quad (\text{S11})$$

$$\sigma_i = \eta \sqrt{\sum_j (B_{ij})^2}, \quad (\text{S12})$$

where the matrix  $B$  has dimensions  $n \times p$  and the resulting vector  $\vec{\sigma}$  contains the standard deviation of noise in each pixel of the reconstructed image, plotted in Fig. 2b of the main text.

### S4. SENSOR ENERGY LANDSCAPE

#### A. Determinant decomposition

To enable systematic design of the sensor configuration, we aim to maximize the determinant of the matrix  $A$  in the reconstruction (S8). The matrix determinant corresponds to the volume of the confidence ellipsoid around the maximal likelihood reconstruction. The choice to maximize the determinant is known as D-optimal design [10, 11], contrasted with A-optimal and E-optimal designs (matrix trace and spectral gap, respectfully).

The general idea of the computation is to relate the (log-) determinant of  $A$  to the locations of the sensors, both in absolute space and with respect to each other. The dependence of sensor placement on absolute coordinates is equivalent to a 1-body interaction, or external field. The dependence of sensor placement on relative positions is equivalent to 2-body, 3-body, and higher order sensor interactions. Below we derive the functional form of interactions to all orders directly from the training data.

We start with transforming the determinant of  $A$  into the determinant of a related matrix by using Sylvester's



determinant theorem:

$$\begin{aligned} \det A &= \det\left(S^{-2} + \frac{\Theta^T \Theta}{\eta^2}\right) \\ &= \det(S^{-2}) \det\left(I + S^2 \frac{\Theta^T \Theta}{\eta^2}\right) \\ &= \det(S^{-2}) \det\left(I + \frac{\Theta S^2 \Theta^T}{\eta^2}\right), \end{aligned} \quad (\text{S13})$$

which converts an  $r \times r$  matrix into a  $p \times p$  matrix, with size directly related to the number of sensors.

To deepen the analogy with energy in physics, we identify the *negative* log-determinant with the Hamiltonian of a sensor set  $\gamma$ :

$$\mathcal{H}(\gamma) \equiv -\ln \det(A) = E_b - \text{Tr} \ln\left(I + \frac{\Theta S^2 \Theta^T}{\eta^2}\right), \quad (\text{S14})$$

where we used the identity  $\ln \det X = \text{tr} \ln X$  for any generic matrix  $X$ .

We identify the expression within the logarithm with an outer product of a matrix with itself  $\Theta S^2 \Theta^T \equiv G_\gamma G_\gamma^T$ . We term the row vectors  $\tilde{g}_i, i \in \gamma$  *sensing vectors*; the matrix  $G_\gamma$  is then assembled from a subset of rows of  $G \equiv \Psi_r S$  that correspond to chosen sensors  $i \in \gamma$ . The goal of the subsequent derivation is to relate  $\mathcal{H}(\gamma)$  to the selected sensing vectors.

## B. Expansion in $\eta$ and resummation

The Hamiltonian expression (S14) requires taking a matrix logarithm of a complex matrix expression. The outer product  $G_\gamma G_\gamma^T$  is a positive-semidefinite matrix, and thus the argument of the logarithm  $I + G_\gamma G_\gamma^T / \eta^2$  is a positive-definite matrix  $\forall \eta$ , and the logarithm always exists. Additionally, for a sufficiently large value of  $\eta$  the logarithm can be represented as an absolutely and uniformly convergent series expansion in  $1/\eta^2$ . The strategy of the derivation is thus as follows: (i) assume  $\eta$  to be small, (ii) rewrite the energy function as a power expansion in orders of  $1/\eta^2$ , (iii) perform series resummation into a different closed-form function, (iv) expand the validity of the new function to arbitrary  $\eta$  via analytic continuation.

## C. Diagonal separation

We decompose the sensor-driven perturbation as a sum of two matrices:

$$G_\gamma G_\gamma^T \equiv D + R, \quad (\text{S15})$$

where  $D$  contains only the diagonal elements of the outer product, and  $R$  contains all non-diagonal elements. Since  $G_\gamma G_\gamma^T$  is a positive-semidefinite matrix, its diagonal  $D$  inherits the same property. Importantly, the two matrices

in this decomposition do not commute  $[D, R] \neq 0$ , and thus the order of their product is important.

In terms of these newly-defined matrices the Hamiltonian takes the following shape:

$$\mathcal{H} = E_b - \text{Tr} \ln\left(I + \frac{1}{\eta^2}(D + R)\right), \quad (\text{S16})$$

where  $E_b \equiv -\text{Tr} \ln(\Sigma_r^{-2})$  is the baseline energy independent of noise and sensor choices. We then expand the matrix in powers of  $1/\eta^2$ :

$$\mathcal{H}(\gamma) = E_b + \text{Tr} \sum_{k=1}^{\infty} \eta^{-2k} (D + R)^k \frac{(-1)^k}{k}, \quad (\text{S17})$$

where we pulled one factor of  $(-1)$  outside of the sum. The sum  $(D + R)^k$  cannot be expanded as the simple binomial formula, because the matrices don't commute  $[D, R] \neq 0$ . Instead, the sum involves many products of  $D, R$  in different order with order-dependent values.

We search for an expression for the Hamiltonian in the following form:

$$\mathcal{H}(\gamma) = E_b + \sum_{s=0}^{\infty} f_s(R), \quad (\text{S18})$$

where  $f_s(R)$  is a function in which  $R$  occurs exactly  $s$  times. We can get the form of  $f_s$  by grouping terms with the same number of occurrences of  $R$  in the full sum of Eqn. S17. We treat separately the cases of  $s = 0$  and  $s > 0$ .

For  $s = 0$ , we want to gather the terms in which the crosstalk matrix  $R$  never occurs. At each order in  $k$ , there is exactly one such term  $D^k$ , which we can resum for all orders of  $k$  with appropriate series prefactors:

$$f_0 = \text{Tr} \sum_{k=1}^{\infty} \eta^{-2k} D^k \frac{(-1)^k}{k} = -\text{Tr} \ln\left(I + \frac{1}{\eta^2} D\right), \quad (\text{S19})$$

which always exists because  $D$  is positive-semidefinite.

## D. Case $s > 0$

Now consider the terms for  $s > 0$ . Omitting the scalar factors, an example would be  $\text{Tr}(DRDDRRDDRD)$  where  $s = 4$ . Note that by the cyclic property of the trace, the sequence can be shifted by repeatedly moving terms from the right end to the left end of the product without changing the value of the trace. Several different sequences then contribute the same value to the energy, and the number of such sequences needs to be carefully computed. For the term of order  $k$  with  $s$  occurrences of the matrix  $R$  there are  $\binom{k}{s}$  terms, but not all of them have the same value.

We can write each contributing term in the following form:

$$\text{Tr} \left( \prod_{i=1}^s R D^{l_i} \right), \quad (\text{S20})$$

so that each occurrence of  $R$  is followed by  $l_i$  copies of  $D$ , where  $l_i$  can be zero or higher. The total number of matrices  $D$  or  $R$  has to add up to  $k$ , which constraints the number of  $D$  that can occur:

$$\sum_{i=1}^s l_i = k - s \quad \Rightarrow \quad l_s = k - s - \sum_{i=1}^{s-1} l_i, \quad (\text{S21})$$

thus summing over all terms at fixed order  $k$  involves only  $s - 1$  independent indices. The total number of terms of order  $k$  is:

$$\binom{k}{s} = \frac{1}{s!} k(k-1) \dots (k-s+1), \quad (\text{S22})$$

where the factor  $k$  accounts for the  $k$  locations in the sequence where the “first” occurrence of  $R$  can happen, and the factor  $s!$  accounts for the redundant overcounting of the choices of the “first”, “second”, and the following occurrences of  $R$ , neither of which affect the value of the trace. The remaining counting factors  $(k-1), (k-2), \dots$  count the terms with different values of the trace. Putting these contributions together, we can write the following expression for  $f_s$ :

$$f_s = \text{Tr} \sum_{k=1}^{\infty} \sum_{\{l\}} \prod_{i=1}^s \eta^{-2(1+l_i)} (R D^{l_i}) \frac{k}{s!} \frac{(-1)^k}{k}, \quad (\text{S23})$$

where the sum over possible sets of  $\{l\}$  obeys the constraint of Eqn. S21. The counting factor  $k$  in the numerator cancels with the factor  $k$  from the series expansion of the logarithm. We can now exchange the order of summation in  $k$  and  $l_i$ : instead of doing a constrained sum in all  $l_i$  that add up to the same  $k$ , we treat them on the same level.

Intuitively, the trace can be thought of as a ring that consists of a sequence of  $D, R$  elements. A ring does not have a beginning or the end, hence the factor  $k$  in the number of rings with identical value of the trace. The subsequent matrices  $R$  are separated by  $l_i$  matrices  $D$ . Instead of counting all possible rings of the same length  $k$ , we instead perform independent sums over the length of all separators  $l_i$ , and the corresponding rings span all possible lengths, similar to enumeration approaches in heterogeneous self-assembly [12, 13]. We thus rewrite

the sum as follows:

$$(-1)^k = (-1)^s \prod_{i=1}^s (-1)^{l_i} \quad (\text{S24})$$

$$\begin{aligned} f_s &= \frac{(-1)^s}{s!} \text{Tr} \sum_{\{l\}} \prod_{i=1}^s \eta^{-2(1+l_i)} R (-D)^{l_i} \\ &= \frac{(-1)^s}{s!} \text{Tr} \prod_{i=1}^s \sum_{l_i=0}^{\infty} \eta^{-2(1+l_i)} R (-D)^{l_i} \\ &= \frac{(-1)^s}{s!} \text{Tr} \left( [\eta^{-2} R (I + \eta^{-2} D)^{-1}]^s \right), \end{aligned} \quad (\text{S25})$$

where between the second and third lines we exchanged the order of product and sum. The resulting sum in powers of  $(-D)$  is an alternating sign geometric series which converges for large  $\eta$ , and the resulting inversion of the diagonal matrix  $(I + \eta^{-2} D)$  is valid for any value of  $\eta$  because  $D$  is positive semi-definite.

We can thus write the Hamiltonian exactly as follows:

$$\begin{aligned} \mathcal{H}(\gamma) &= E_b - \text{Tr} \ln(I + \eta^{-2} D) \\ &\quad + \sum_{s=1}^{\infty} \frac{(-1)^s}{s!} \text{Tr} \left( [\eta^{-2} R (I + \eta^{-2} D)^{-1}]^s \right), \end{aligned} \quad (\text{S26})$$

which is a surprisingly concise form in terms of the separated diagonal and off-diagonal terms. If we were to rewrite the matrix expression in index notation, the  $s = 0$  term would have a single sum over all sensors, and each further term  $s$  have a sum over  $s$ -sensor interactions. Note that since  $R$  is non-diagonal and  $(I + D)^{-1}$  is diagonal, the  $s = 1$  term is a trace of a non-diagonal matrix and thus it always vanishes. Only the terms for higher  $s > 1$  have nonzero values. Since the matrix  $R$  does not have a general sign-definite property, the resulting series does not approximate energy either from above or from below.

## E. Energy landscapes

Here we rewrite the matrix expression of Eqn. S26 in index notation to highlight the contributions of 1-sensor and 2-sensor terms. First note the following index representation based on Eqn. S15:

$$(D + R)_{ij} = (G_{\gamma} G_{\gamma}^T)_{ij} = \vec{g}_i \cdot \vec{g}_j, \quad (\text{S27})$$

where we highlight the nature of the terms as dot products of sensing vectors  $\vec{g}_i$ . The diagonal terms  $D$  correspond to the dot product of each  $\vec{g}_i$  with *itself*, while the off-diagonal terms  $R$  correspond to the dot products with *different* vectors.

We now need to convert the understanding of the  $\vec{g}_i$  vectors into the Ising-like Hamiltonian of shape in Eqn. S14. We ignore the term  $E_b$  since it does not depend on the noise or the choice of the sensors. We can also drop the  $s = 1$  term of the sum since it vanishes

because of our matrix decomposition choices. We then truncate the sum in  $s$  to only include the term  $s = 2$ , resulting in the following expression for the 2-point energy:

$$\mathcal{H}_{2pt}(\gamma) \equiv -\text{Tr} \ln(I + D/\eta^2) + \frac{1}{2} \text{Tr} \left( [\eta^{-2} R (I + \eta^{-2} D)^{-1}]^2 \right), \quad (\text{S28})$$

which we need to transform into the index notation.

The first term has a trace of the log of a diagonal matrix, and thus equals to the sum of the logs of the individual entries:

$$-\text{Tr} \ln(I + \eta^{-2} D) = \sum_{i \in \gamma} \ln(1 + D_i/\eta^2) = \sum_{i \in \gamma} \ln(1 + \vec{g}_i \cdot \vec{g}_i/\eta^2), \quad (\text{S29})$$

which is a sum of 1-sensor terms.

The second term can be rewritten as follows:

$$\begin{aligned} & \frac{1}{2} \text{Tr} \left( [\eta^{-2} R (I + \eta^{-2} D)^{-1}]^2 \right) \\ &= \frac{1}{2} \sum_{ij \in \gamma} \frac{R_{ij} R_{ji} / \eta^4}{(1 + D_i/\eta^2)(1 + D_j/\eta^2)} \\ &= \frac{1}{2} \sum_{i \neq j \in \gamma} \frac{(\vec{g}_i \cdot \vec{g}_j)^2 / \eta^4}{(1 + \vec{g}_i \cdot \vec{g}_i/\eta^2)(1 + \vec{g}_j \cdot \vec{g}_j/\eta^2)}, \end{aligned} \quad (\text{S30})$$

where we used the fact that  $R$  is non-diagonal to restrict the sum to only run over the sensor pairs with indices  $i \neq j$ . For both the 1-sensor and the 2-sensor terms, the sums run only over the sensors in the chosen set  $\gamma$ . We can thus extend the computation of the terms to the whole landscape that can be analyzed to pick the sensors that optimize the energy. The resulting landscape has the following form for all  $ij$ :

$$\mathcal{H}_{2pt}(\gamma) = \sum_{i \in \gamma} h_i + \sum_{i \neq j \in \gamma} J_{ij} \quad (\text{S31})$$

$$h_i \equiv -\ln(1 + \vec{g}_i \cdot \vec{g}_i/\eta^2) \leq 0 \quad (\text{S32})$$

$$J_{ij} \equiv \frac{1}{2} \frac{(\vec{g}_i \cdot \vec{g}_j)^2 / \eta^4}{(1 + \vec{g}_i \cdot \vec{g}_i/\eta^2)(1 + \vec{g}_j \cdot \vec{g}_j/\eta^2)} \geq 0, \quad (\text{S33})$$

which is valid for any  $\eta$ .

What are the limits of this energy approximation? The answer to this question is intimately tied to the sensor placement algorithm. Generically, we expect the approximation to work while  $\vec{g}_i \cdot \vec{g}_j \ll \vec{g}_i \cdot \vec{g}_i$ , i.e. the correlation between the sensing vectors is small compared with their magnitude. For many systems it should be possible to choose sensors  $i, j$  so that the terms  $J_{ij}$  are small compared to the terms  $h_i$ . However, the *number* of crosstalk terms  $J_{ij}$  for  $p$  sensors grows as  $p^2$  with sensor number  $p$ . While the individual terms might be small, with increasing number of desired sensors both the number of terms grows, and the algorithm runs out of low crosstalk locations. Due to the combination of these reasons, we

expect the approximation to inevitably break down for large number of sensors  $p$ . How large that number is would depend on the properties of the training data and the placement domain, and thus would need to be established in numerical experiments.

We note that the higher-order terms would have the shape similar to  $J_{ij}$  in Eqn. S33, with a large number of indices. Due to the construction of  $R$  as a non-diagonal matrix, the terms where *adjacent* indices are identical would correspond to the diagonal of  $R$  and thus vanish. However, the indices can repeat in non-adjacent positions, e.g. at fourth order in  $J_{ijij}^{(4)} \neq 0$ . The 2-point expression Eqn. S31 is thus not exact even for placement of 2 sensors, but is expected to be a good approximation.

## S5. NOISE LIMITS

### A. High and low noise limits

Here we consider the high noise and low noise limits of the landscape (S32),(S33). In the high noise limit  $\eta \gg 1$  we get:

$$h_i = \mathcal{O}(\eta^{-2}) \quad (\text{S34})$$

$$J_{ij} = \mathcal{O}(\eta^{-4}), \quad (\text{S35})$$

so the crosstalk falls off faster than the 1-sensor landscape. On one side, this stimulates putting more sensors in the basin of lowest  $h_i$ : since sensor noise is high, it makes more sense to collect measurements in the location of highest signal variance. On the other side, placing sensors close by breaks the approximation condition  $\vec{g}_i \cdot \vec{g}_j \ll \vec{g}_i \cdot \vec{g}_i$ , leading to a faster divergence between the 2-point energy and the true energy.

In the low noise limit  $\eta \ll 1$ :

$$h_i = 2 \ln(\eta) - \ln(\vec{g}_i \cdot \vec{g}_i) \quad (\text{S36})$$

$$J_{ij} = \frac{1}{2} \frac{(\vec{g}_i \cdot \vec{g}_j)^2}{(\vec{g}_i \cdot \vec{g}_i)(\vec{g}_j \cdot \vec{g}_j)}, \quad (\text{S37})$$

which approaches a constant, noise-independent shape where neither the 1-point nor 2-point or higher order interactions vanish for a generic sensor set. It should still be possible to choose a small set of sensors with low crosstalk and ensure that the 2-point energy is a good approximation of the true energy. Importantly, in low noise limit the sensor placement landscape does not depend on the absolute magnitude of the prior, but does depend on its shape, i.e. uniform and non-uniform priors would typically result in different landscapes and thus different chosen sensor sets.

## S6. SENSOR PLACEMENT METHODS

We consider and compare four algorithms of sensor placement:

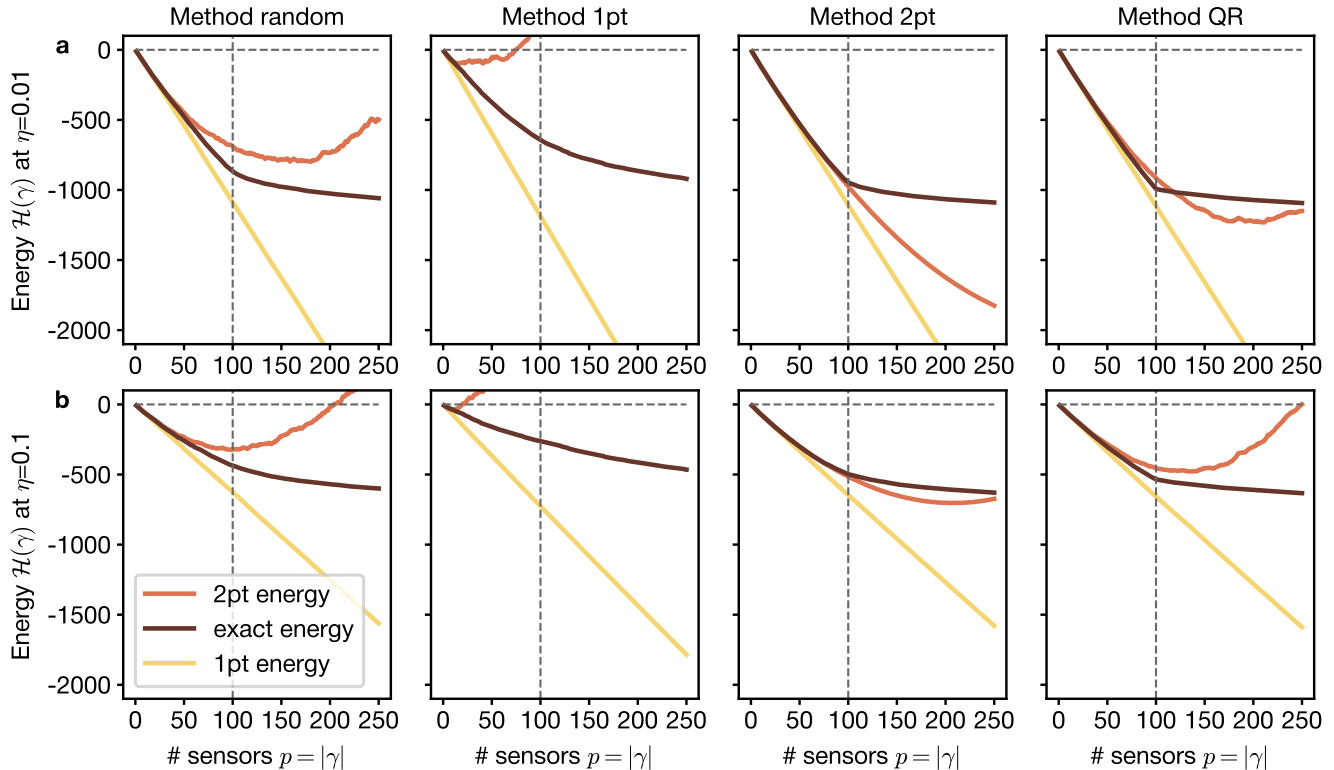


FIG. S2. Comparison of sensor placement methods for the Olivetti faces dataset as measured by different energy expressions. The rows (a) and (b) use the energy landscape at different values of noise  $\eta$ , the columns correspond to four different sensor placement methods. The curves correspond to three energy formulae. Exact energy is evaluated by directly computing the determinant in Eqn. (S14), ignoring the constant term  $E_b$ . 2-point energy is evaluated with Eqn. S28. 1-point energy is evaluated by taking only the first term in Eqn. S28. The horizontal dashed line indicates  $\mathcal{H} = 0$ , the vertical line indicates the reconstruction rank  $p = r$ .

1. *Random algorithm*: sensors are placed uniformly randomly within the signal domain without overlap.
2. *1-point algorithm*: sensors are placed to greedily minimize the 1-point energy  $h_q$  without overlap.
3. *2-point algorithm*: sensors are placed to greedily minimize the 2-point energy following Eqn. 6 of main text without overlap.
4. *QR algorithm*: sensors are placed via greedy QR factorization of the  $\Theta_r$  matrix with the `PySensors` package [14].

The goal of all four methods is to minimize the sensor configuration energy  $\mathcal{H}(\gamma)$  by minimizing different proxies (Fig. S2). Across all methods, exact energy is higher than 1-point energy, indicating the importance of taking sensor crosstalk into account. For the 2-point and QR methods, the 2-point energy is a close approximation for the exact energy up until the number of sensors reaches the reconstruction rank  $p = r$ . For the 1-point method, the discrepancy between the exact and 2-point energies

is the highest since placing the sensors without considering crosstalk results in strong spatial clustering and thus large crosstalk. The 1-point method consequently has the worst reconstruction RMSE (Fig. 3c of the main text). The random placement method has performance better than 1-point and worse than 2-point and QR.

## S7. PRIOR SELECTION

The reconstruction formula (S8) and the sensor energy landscape both depend on the choice of the prior variances  $S$ . We consider the prior to be Gaussian, but it can have different patterns of variances along each dimension: either it is flat  $S = \sigma I$  (we choose  $\sigma = 10^3$ ), or it follows the singular values of the dataset  $S = \Sigma_r$ . Since there are two choices of prior for two different operations, we need to consider four possible combinations.

Along with the prior-regularized reconstruction we consider a direct reconstruction of the latent state vector

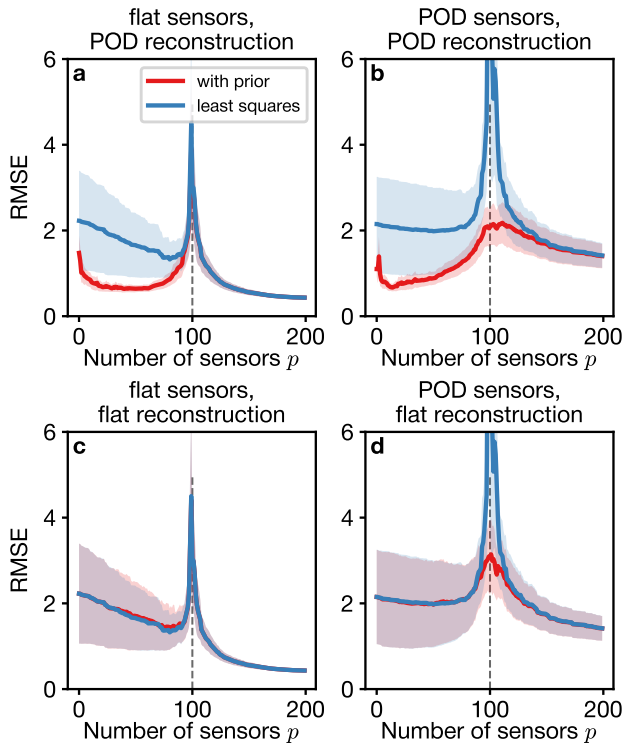


FIG. S3. RMSE benchmark to select the combination of priors. Columns correspond to the choice of prior for sensor placement at noise level  $\eta = 0.1^\circ C$ , rows correspond to the choice of prior for reconstruction. Red curves correspond to the reconstruction with the corresponding prior, while blue curves correspond to the least-squares reconstruction. The solid line and shaded region indicating average  $\pm 1$  standard deviation across the test set.

$\hat{\vec{a}}$  that solves a linear least square problem:

$$\hat{\vec{a}} = \arg \min_{\vec{a}} \|\vec{y} - \Theta \vec{a}\|, \quad (\text{S38})$$

which is well-defined for any number of sensors  $p$ .

We show the benchmark comparison in Fig. S3. The least squares reconstruction is never better than regularized reconstruction. In case of a flat prior used for regularization, the RMSE curves are almost equivalent except for the peak at  $p \sim r$  that is suppressed by regularization. Selection of sensors is better performed against a flat prior (left column), leading to spread-out sampling and thus lower RMSE in the oversampled regime  $p > r$ . Sensors selected against a flat prior are sensitive to all modes used in the reconstruction similar to the QR method [11], while sensors selected against a POD prior are primarily sensitive the first few modes. Reconstruction is better performed with a POD prior (top row) since it leads to a much smaller and less variable RMSE in the undersampled regime  $p < r$ .

Following the conclusions of this benchmark test, we pick sensors against a flat prior, yet reconstruct states

with the POD prior. This combination of methods is used for all results reported in the main text and Figs. S4-S5.

## S8. SENSOR PLACEMENT FOR OLIVETTI FACES

Fig. S4 shows the sensor placement and reconstruction for the Olivetti faces dataset. The sensors cluster around the areas of high variability in human faces: eyes, nose, lips, as well as corners of the image. In contrast, there are almost no sensors on the forehead and cheeks which vary very little between the images. This dataset also suffers from reconstruction instability at  $r \sim p$  caused by the truncation of POD modes.

## S9. SENSOR PLACEMENT FOR CYLINDER FLOW

Fig. S5 shows the sensor placement and reconstruction for the cylinder flow dataset. The sensors cluster primarily in the wake behind the cylinder, with a few appearing at the far edge of the image. This dataset does not suffer from reconstruction instability at  $r \sim p$  since the POD modes were truncated at a very low singular value.

## S10. EXHAUSTIVE SENSOR ENUMERATION

Figs. 3,S2 establish the near-equivalence of the 2-point algorithm and the QR algorithm for sensor placement, but both algorithms are approximate optimizers. For  $p$  sensors in  $n$ -dimensional state space there exist  $\binom{n}{p}$  possible configurations that can be enumerated directly for small  $n, p$ . In Figs. S6,S7 we enumerate all sensor configurations for the GFF and RSS datasets, respectively, which both have  $n = 25$  and  $p \in [1, 8]$ .

We assess the degree of optimality of the two algorithms with three metrics. First, we compute the Spearman rank correlation  $\rho$  between the exact and approximate 2-point energies, which indicates to what degree minimizing the 2-point energy (moving down on the two-dimensional histograms) is equivalent to minimizing the true energy (moving left on the histograms). The Spearman correlation stays at the level of  $\rho > 0.99$  to two significant figures, showing that the exact energy is well approximated by the 2-point energy for all sensor configurations.

Second, we compute is efficiency  $Q$ , equal to the fraction of the sensor configurations with exact energy equal or higher than the configuration found by a particular method. For the best solution found by brute force search, efficiency is by definition  $Q = 100\%$ . Across both datasets, efficiency of the 2-point and QR methods reaches that level, indicating that both methods find the exact optimal sensor configuration.

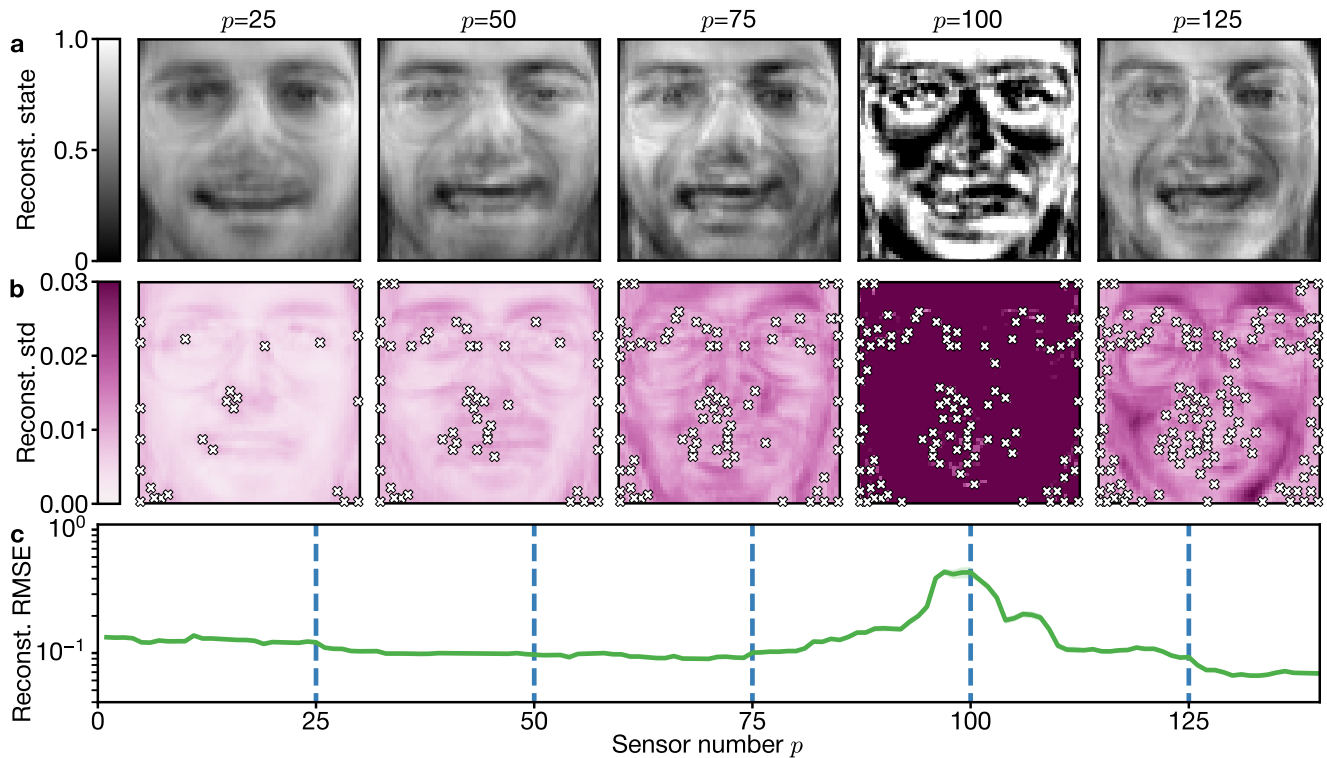


FIG. S4. Reconstruction of Olivetti faces with data-driven sensor placement with  $r = 100$  modes and noise  $\eta = 0.01$ . (a) Maximal likelihood reconstruction. (b) Reconstruction uncertainty heatmap with white crosses marking the sensors selected by the 2-point algorithm. (c) Root mean square error (RMSE) of state reconstruction, with solid line and shaded region indicating average  $\pm 1$  standard deviation across the test set. The vertical dashed lines indicates the sensor counts for the reconstructions shown in (a)-(b).

Third, we compute the energy difference between the true minimum and the approximations (Figs. S6i,S7i) that remains at the level of floating point number precision.

An important limitation of this comparison is the artificially small size of the GFF and RSS datasets. While it is easy to generate larger datasets with the same software, they would not be amenable to brute force enumeration. Within the empirical datasets such as the Sea

Surface Temperature, it is easy to place sensors with low crosstalk (Fig. 1 of main text) since crosstalk typically falls off with spatial distance between sensor locations. For small datasets, there are no locations with large distance between them, and thus it is impossible to achieve low crosstalk. We are looking forward to future methods for comparing the exact and approximately optimal sensor configurations.

- 
- [1] B. Huang, C. Liu, V. Banzon, E. Freeman, G. Graham, B. Hankins, T. Smith, and H.-M. Zhang, Improvements of the daily optimum interpolation sea surface temperature (doisst) version 2.1, *Journal of Climate* **34**, 2923 (2021).
  - [2] At the time of writing the dataset was available via the Physical Sciences Laboratory at <https://psl.noaa.gov/data/gridded/data.noaa.oisst.v2.html>.
  - [3] F. S. Samaria and A. C. Harter, Parameterisation of a stochastic model for human face identification, in *Proceedings of 1994 IEEE workshop on applications of computer vision* (IEEE, 1994) pp. 138–142.
  - [4] K. Taira and T. Colonius, The immersed boundary method: a projection approach, *Journal of Computational Physics* **225**, 2118 (2007).
  - [5] T. Colonius and K. Taira, A fast immersed boundary method using a nullspace approach and multi-domain far-field boundary conditions, *Computer Methods in Applied Mechanics and Engineering* **197**, 2131 (2008).
  - [6] C. Cadiou, *Fyeldgenerator* (2022).
  - [7] S. Fuller, B. Greiner, J. Moore, R. Murray, R. van Paassen, and R. Yorke, The python control systems library (python-control), in *2021 60th IEEE Conference on Decision and Control (CDC)* (IEEE, 2021) pp. 4875–

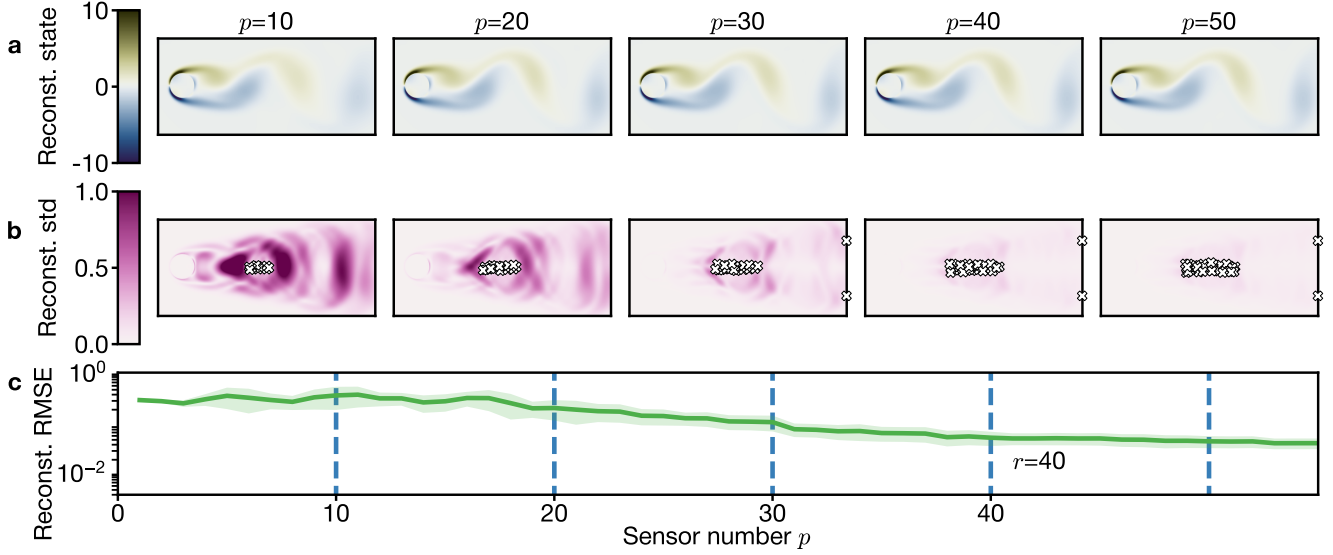


FIG. S5. Reconstruction of cylinder flow with data-driven sensor placement with  $r = 40$  modes and noise  $\eta = 0.1$ . (a) Maximal likelihood reconstruction. (b) Reconstruction uncertainty heatmap with white crosses marking the sensors selected by the 2-point algorithm. (c) Root mean square error (RMSE) of state reconstruction, with solid line and shaded region indicating average  $\pm 1$  standard deviation across the test set. The vertical dashed lines indicates the sensor counts for the reconstructions shown in (a)-(b).

4881.

- [8] R. Everson and L. Sirovich, Karhunen–loève procedure for gappy data, *JOSA A* **12**, 1657 (1995).
- [9] S. E. Otto and C. W. Rowley, Inadequacy of linear methods for minimal sensor placement and feature selection in nonlinear systems: a new approach using secants, *Journal of Nonlinear Science* **32**, 69 (2022).
- [10] P. F. de Aguiar, B. Bourguignon, M. Khots, D. Massart, and R. Phan-Thau-Luu, D-optimal designs, *Chemometrics and intelligent laboratory systems* **30**, 199 (1995).
- [11] K. Manohar, B. W. Brunton, J. N. Kutz, and S. L. Brunton, Data-driven sparse sensor placement for reconstruction: Demonstrating the benefits of exploiting known patterns, *IEEE Control Systems Magazine* **38**, 63 (2018).
- [12] A. Murugan, J. Zou, and M. P. Brenner, Undesired usage and the robust self-assembly of heterogeneous structures, *Nature communications* **6**, 6203 (2015).
- [13] A. A. Klishin and M. P. Brenner, Topological design of heterogeneous self-assembly, arXiv preprint arXiv:2103.02010 (2021).
- [14] B. M. de Silva, K. Manohar, E. Clark, B. W. Brunton, S. L. Brunton, and J. N. Kutz, Pysensors: A python package for sparse sensor placement, arXiv preprint arXiv:2102.13476 (2021).

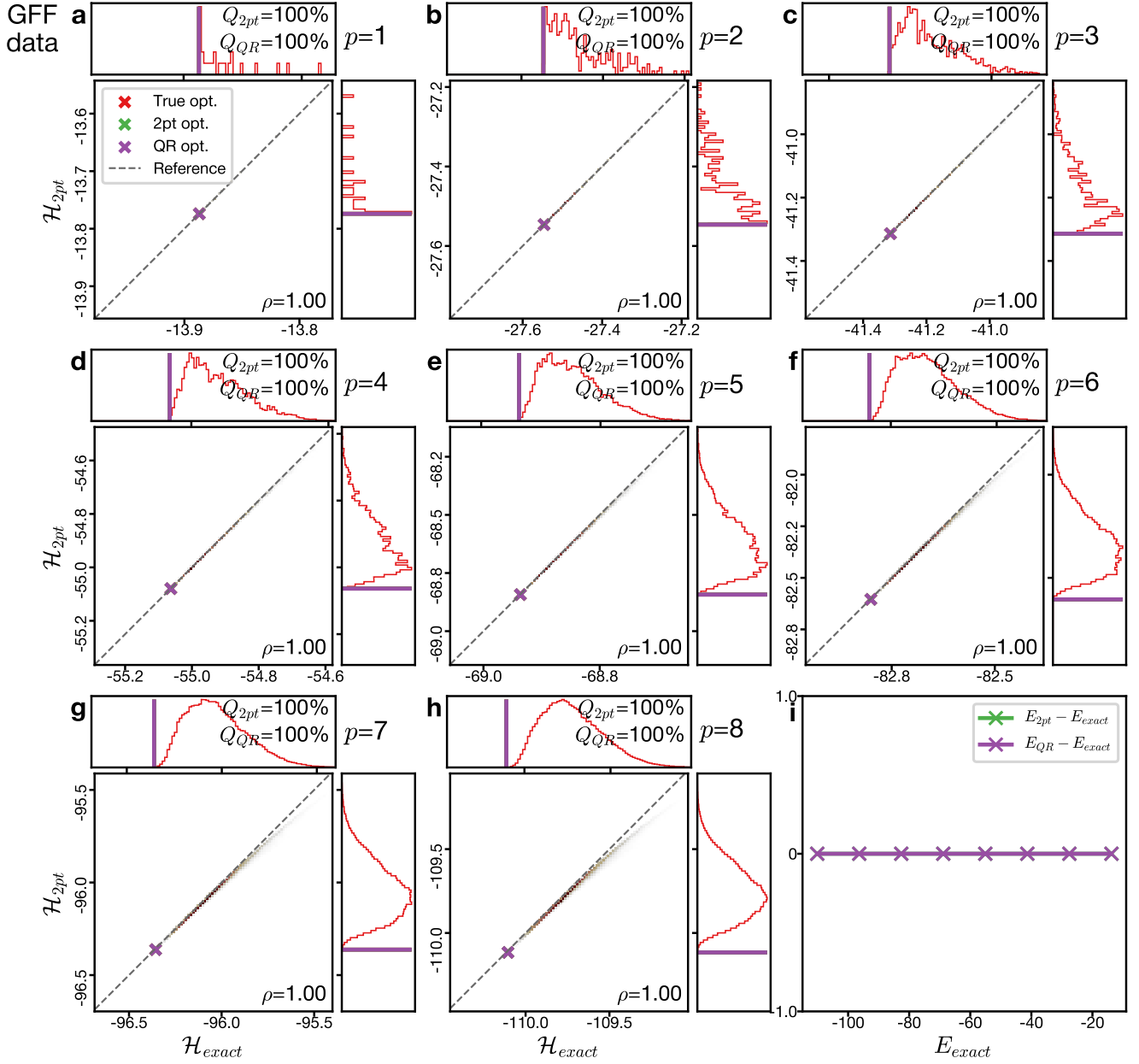


FIG. S6. Comparison of sensor configurations between brute force search, 2-point algorithm, and QR methods for the GFF dataset. (a-h) Two-dimensional histograms of the joint distribution in the exact energy (S14) and 2-point energy (S28) for all configurations with sensor number  $p \in [1, 8]$ . The value of  $\rho$  corresponds to the Spearman correlation between the two energies. The right and top panels show the marginal histogram in only one of the variables. The crosses indicate the sensor configurations found by each of the three methods. (i) The discrepancy in energy between the absolute and approximate minima found by the two methods. Lower exact energy corresponds to more sensors.



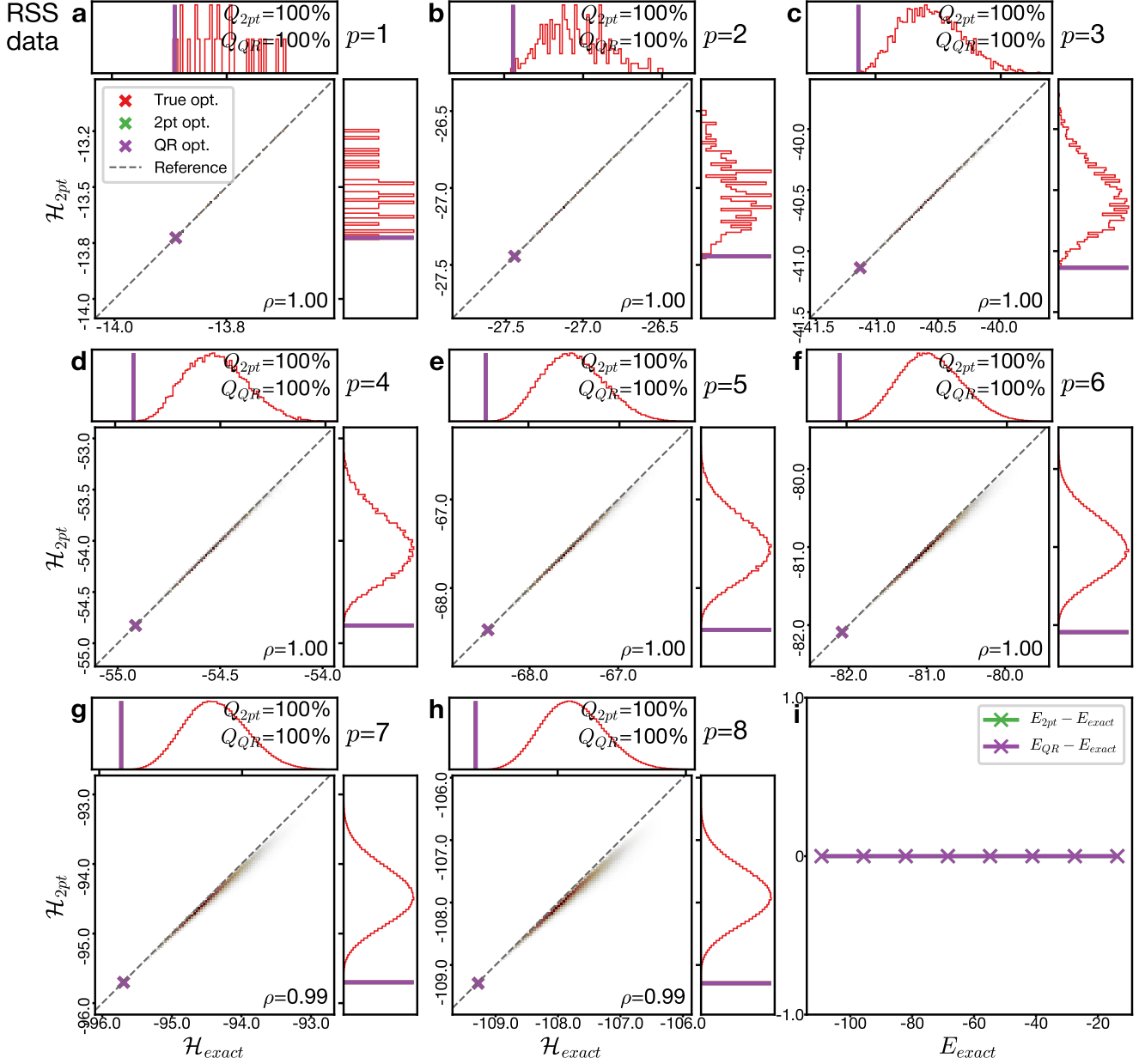


FIG. S7. Comparison of sensor configurations between brute force search, 2-point algorithm, and QR methods for the RSS dataset. (a-h) Two-dimensional histograms of the joint distribution in the exact energy (S14) and 2-point energy (S28) for all configurations with sensor number  $p \in [1, 8]$ . The value of  $\rho$  corresponds to the Spearman correlation between the two energies. The right and top panels show the marginal histogram in only one of the variables. The crosses indicate the sensor configurations found by each of the three methods. (i) The discrepancy in energy between the absolute and approximate minima found by the two methods. Lower exact energy corresponds to more sensors.